Edge-to-edge Cohesive Shell Elements in LS-DYNA

Jesper Karlsson[1], Martin Fagerström[2]

[1]Dynamore Nordic AB
[2]Chalmers University of Technology

1 Introduction

Cohesive elements are an important tool for simulating the propagation of cracks in materials. For example, to describe failure propagation in a thin walled sheet metal structure along an *a priori* known crack path, e.g. along a weld line, through-the-thickness crack propagation has in the literature been modeled by embedding interface cohesive zone elements in between shells elements, see e.g. References [2,3,4,7,8].

By connecting faces and edges of neighboring elements, the cohesive elements are used to describe the degrading load carrying capacity of the material in the evolving fracture process zone. The elements do not, however, model a physical material in a continuum mechanics sense; instead they model a (non-linear dissipative) spring based force response depending on the separation of the neighboring faces and edges through a cohesive law. Hence, they can remain stable under zero or negative volume.

LS-DYNA has a variety of solid cohesive elements to simulate cracks between solids (element type 19 and 21) and delamination of shells (type 20 and 22). Elements 19 and 20 are hexahedral elements and 21 and 22 are corresponding wedge/pentahedral elements. While elements 19 and 21 use a total formulation where the separation between layers is calculated directly from the interpolation of nodal coordinates, elements 20 and 22 require the use of an incremental formulation to account for objectivity issues related to the rotational degrees of freedoms in shells. As of Revision 8.0 a new cohesive shell element is now available for edge-to-edge connection of quadrilateral thin shells, based on the same principles of incrementation as in cohesive elements 20 and 22. The new cohesive element (type 29) accounts for in-plane and out-of-plane separation as well as hinge bending and works with existing cohesive material models.

2 Usage

The new shell element 29 is available as **ELFORM=29** on the ***SECTION_SHELL** card. It supports all cohesive materials that are available for solid cohesive elements, and supports both SMP, MPP, as well as implicit dynamics. To support hinge bending, four integration points are always used, and the option **NIP** on ***SECTION_SHELL** is thus not supported.

Since in-plane rotation of neighboring shells will not induce translational velocities in the integration points of the cohesive layer, a stabilization scheme is applied, so called *drilling rotation constraints*. This artificial stabilization can be adjusted by the **DRCPM** parameter on the ***CONTROL_SHELL** or ***CONTROL_IMPLICIT_SOLVER** cards.

3 Theory

Cohesive shell element 29 connects the edges of two thin shells via a cohesive law. Figure 1 shows a schematic of the cohesive shell and its neighboring elements. The cohesive element is here defined by the vertices m_4, m_3, n_2, n_1, with local coordinate system $(\boldsymbol{q}_1, \boldsymbol{q}_2, \boldsymbol{q}_3)$, and all elements are assumed to be of equal thickness t. Perpendicular to the cohesive shell, located in between the top and bottom elements in the $(\boldsymbol{q}_1, \boldsymbol{q}_2)$-plane, is the cohesive layer. In this layer the separation distance between the adjacent surfaces of the (in thickness direction extruded) top and bottom elements is calculated. To account for bending, the separation distance is here computed in four integration points in the cohesive layer, giving rise to forces and moments in the cohesive element vertices through a cohesive law.

In the following subsections the connection between the separation distance and the resulting nodal forces is explained in detail.
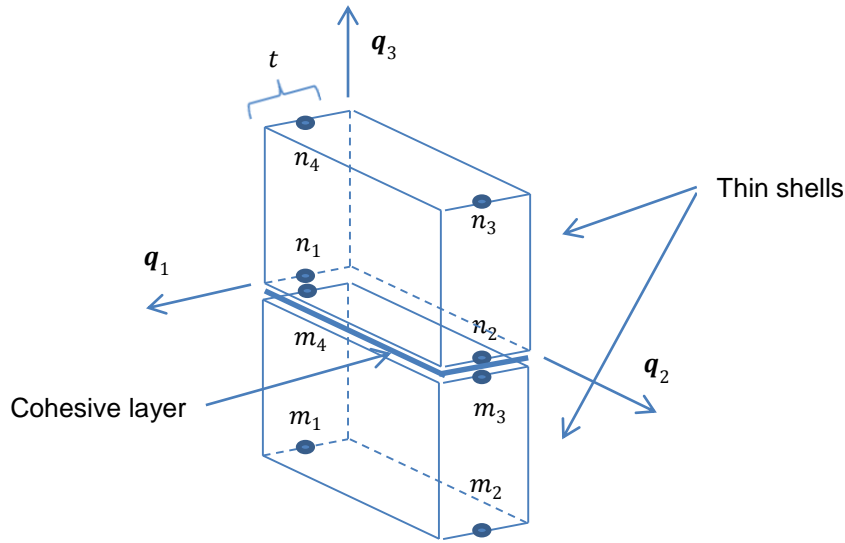
Fig.1: Schematics of cohesive element (nodes m_4, m_3, n_2, n_1) and neighboring shell elements.

3.1 Kinematics

The separation distance in the cohesive layer is defined by

$$d = Q^T(x_t - x_b) - d_0, \tag{1}$$

where

$$Q = [q_1 \quad q_2 \quad q_3], \tag{2}$$

is the local coordinate system and

$$\mathbf{x}_t = \left\{\mathbf{x}_1^n + \xi\frac{t}{2}\boldsymbol{n}_t\right\}\frac{1-\eta}{2} + \left\{\mathbf{x}_2^n + \xi\frac{t}{2}\boldsymbol{n}_t\right\}\frac{1+\eta}{2},$$
$$\mathbf{x}_b = \left\{\mathbf{x}_4^m + \xi\frac{t}{2}\boldsymbol{n}_b\right\}\frac{1-\eta}{2} + \left\{\mathbf{x}_3^m + \xi\frac{t}{2}\boldsymbol{n}_b\right\}\frac{1+\eta}{2}, \tag{3}$$

are global coordinates on the top and bottom surfaces of the extruded shells for a given iso-parametric coordinate $(\xi,\eta) \in [-1,1] \times [-1,1]$. The neighboring top and bottom shell normals are denoted $\boldsymbol{n}_t$ and $\boldsymbol{n}_b$, respectively, and the distance vector $\boldsymbol{d}_0$ represents the initial gap for cases where the cohesive interface has a nonzero thickness, so initially $\boldsymbol{d} = \boldsymbol{0}$. Also, the thickness of the neighboring shells assumed to be constant and equal to t.

From here and onwards, superscripts *n* and *m* denote the top and bottom surfaces, respectively, and thus $\boldsymbol{x}_i^n$ and $\boldsymbol{x}_i^m$ are the nodal coordinates associated with the two surfaces.

For cohesive element 29, the separation $\boldsymbol{d}$ is updated using an incremental formulation

$$\dot{\boldsymbol{d}} = \boldsymbol{Q}^T(\dot{x}_t - \dot{x}_b) + \dot{\boldsymbol{Q}}^T(x_t - x_b), \tag{4}$$

where

$$\dot{\boldsymbol{x}}_t = \left\{\dot{x}_1^n + \xi\frac{t}{2}\boldsymbol{\omega}_1^n \times \boldsymbol{n}_t\right\}\frac{1-\eta}{2} + \left\{\dot{x}_2^n + \xi\frac{t}{2}\boldsymbol{\omega}_2^n \times \boldsymbol{n}_t\right\}\frac{1+\eta}{2},$$
$$\dot{\boldsymbol{x}}_b = \left\{\dot{x}_4^m + \xi\frac{t}{2}\boldsymbol{\omega}_4^m \times \mathbf{n}_b\right\}\frac{1-\eta}{2} + \left\{\dot{x}_3^m + \xi\frac{t}{2}\boldsymbol{\omega}_3^m \times \mathbf{n}_b\right\}\frac{1+\eta}{2}. \tag{5}$$

In these equations, $\boldsymbol{\omega}_i^m$ and $\boldsymbol{\omega}_i^n$ denote nodal rotational velocities. Note that for evaluation the velocities of x_t and x_b it is assumed that the fibers pointing from the assumed mid layers of the neighboring shells coincides with the corresponding shell normals $\boldsymbol{n}_t$ and $\boldsymbol{n}_b$. This is in analogy to how

the Belytschko-Tsay element is treating the fiber vectors and presumably enhances robustness of the elements.

The local coordinate system is computed by

$$q_2 = \frac{x_2^n + x_3^m - x_1^n - x_4^m}{|x_2^n + x_3^m - x_1^n - x_4^m|}, \tag{6}$$

followed by

$$q = x_4^n + x_3^n - x_1^m - x_2^m, \tag{7}$$

$$q_3 = \frac{q - q_2 q^T q_2}{|q - q_2 q^T q_2|}, \tag{8}$$

and

$$q_1 = q_2 \times q_3. \tag{9}$$

3.2 Constitutive law

The cohesive constitutive law determines the normal and shear stress, expressed here as the traction vector t as a function of the separation vector d, *i.e.* $t = t(d, \dots)$. The components of the traction vector correspond to the projection of stress onto the mid layer normal q_3 and the tangential plane (q_1, q_2). Typical appearance of each component of this vector is illustrated in Figure 2, where the cohesive interface behaves elastically up to a critical separation distance d_e and peak stress t_e after which damage commences. The interface is damaged and failure occurs at a certain critical separation distance d_c, the unloading is typically elastic with the secant modulus as indicated by the dashed arrow.
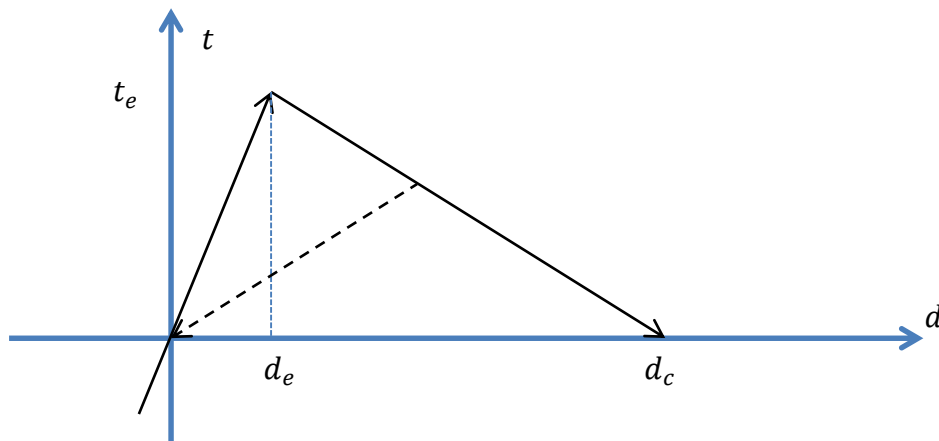

Fig.2:   Common stress versus separation for a cohesive interface

3.3 Nodal forces

The principle of virtual work states that (sum over *i*)

$$\int_A \dot{d}^T \sigma \, dA = \{\dot{x}_i^m\}^T f_i^m + \{\dot{x}_i^n\}^T f_i^n + \{\omega_i^m\}^T r_i^m + \{\omega_i^n\}^T r_i^n, \tag{10}$$

where f_i^j and r_i^j is the nodal force and moment for node i on element j, respectively. The area A represents the cohesive mid layer spanned by the iso-parametric representation and this is used to identify the nodal forces and moments.

From Equation (4) the left hand side of (10) can also be expressed as

$$\int_A \dot{\boldsymbol{d}}^T \boldsymbol{\sigma} dA = \int_A \dot{\boldsymbol{x}}_t^T \boldsymbol{Q} \boldsymbol{\sigma} dA - \int_A \dot{\boldsymbol{x}}_b^T \boldsymbol{Q} \boldsymbol{\sigma} dA - \int_A \boldsymbol{d}^T \dot{\boldsymbol{Q}}^T \boldsymbol{Q} \boldsymbol{\sigma} dA. \tag{11}$$

Before continuing, rewrite (5) as

$$\dot{\boldsymbol{x}}_t^T = \{\dot{\boldsymbol{x}}_1^n\}^T \frac{1-\eta}{2} - \{\boldsymbol{\omega}_1^n\}^T \boldsymbol{R}_t^T \frac{1-\eta}{2} \xi \frac{t}{2} + \{\dot{\boldsymbol{x}}_2^n\}^T \frac{1+\eta}{2} - \{\boldsymbol{\omega}_2^n\}^T \boldsymbol{R}_t^T \frac{1+\eta}{2} \xi \frac{t}{2},$$

$$\dot{\boldsymbol{x}}_b^T = \{\dot{\boldsymbol{x}}_4^m\}^T \frac{1-\eta}{2} - \{\boldsymbol{\omega}_4^m\}^T \boldsymbol{R}_b^T \frac{1-\eta}{2} \xi \frac{t}{2} + \{\dot{\boldsymbol{x}}_3^m\}^T \frac{1+\eta}{2} - \{\boldsymbol{\omega}_3^m\}^T \boldsymbol{R}_b^T \frac{1+\eta}{2} \xi \frac{t}{2}, \tag{12}$$

where $\boldsymbol{R}_*$ is the linear operator defined by

$$\boldsymbol{R}_* \boldsymbol{\omega} = \boldsymbol{n}_* \times \boldsymbol{\omega}. \tag{13}$$

Inserting (12) into the right of (11) gives after some simplifications

$$\int_A \dot{\boldsymbol{d}}^T \boldsymbol{\sigma} dA = -\int_A \boldsymbol{d}^T \dot{\boldsymbol{Q}}^T \boldsymbol{Q} \boldsymbol{\sigma} dA$$

$$+ \{\dot{\mathbf{x}}_1^n\}^T \int_A \left(\frac{1-\eta}{2}\right) \boldsymbol{Q} \boldsymbol{\sigma} dA + \{\boldsymbol{\omega}_1^n\}^T \int_A \left(-\frac{1-\eta}{2} \xi \frac{t}{2}\right) \boldsymbol{R}_t^T \boldsymbol{Q} \boldsymbol{\sigma} dA$$

$$+ \{\dot{\boldsymbol{x}}_2^n\}^T \int_A \left(\frac{1+\eta}{2}\right) \boldsymbol{Q} \boldsymbol{\sigma} dA + \{\boldsymbol{\omega}_2^n\}^T \int_A \left(-\frac{1+\eta}{2} \xi \frac{t}{2}\right) \boldsymbol{R}_t^T \boldsymbol{Q} \boldsymbol{\sigma} dA \tag{14}$$

$$+ \{\dot{\boldsymbol{x}}_4^m\}^T \int_A \left(-\frac{1-\eta}{2}\right) \boldsymbol{Q} \boldsymbol{\sigma} dA + \{\boldsymbol{\omega}_4^m\}^T \int_A \left(\frac{1-\eta}{2} \xi \frac{t}{2}\right) \boldsymbol{R}_b^T \boldsymbol{Q} \boldsymbol{\sigma} dA$$

$$+ \{\dot{\boldsymbol{x}}_3^m\}^T \int_A \left(-\frac{1+\eta}{2}\right) \boldsymbol{Q} \boldsymbol{\sigma} dA + \{\boldsymbol{\omega}_3^m\}^T \int_A \left(\frac{1+\eta}{2} \xi \frac{t}{2}\right) \boldsymbol{R}_b^T \boldsymbol{Q} \boldsymbol{\sigma} dA.$$

If the first term on the right hand side of (14) is neglected we can, using (10) and (14), identify the nonzero nodal forces and moments

$$\boldsymbol{f}_1^n = \int_A \left(\frac{1-\eta}{2}\right) \boldsymbol{Q} \boldsymbol{\sigma} dA, \quad \boldsymbol{f}_2^n = \int_A \left(\frac{1+\eta}{2}\right) \boldsymbol{Q} \boldsymbol{\sigma} dA, \quad \boldsymbol{f}_3^m = -\boldsymbol{f}_2^n, \quad \boldsymbol{f}_4^m = -\boldsymbol{f}_1^n, \tag{15}$$

and

$$\boldsymbol{r}_1^n = -\frac{t}{2} \int_A \left(\frac{1-\eta}{2} \xi\right) \boldsymbol{R}_t^T \boldsymbol{Q} \boldsymbol{\sigma} dA, \quad \boldsymbol{r}_2^n = -\frac{t}{2} \int_A \left(\frac{1+\eta}{2} \xi\right) \boldsymbol{R}_t^T \boldsymbol{Q} \boldsymbol{\sigma} dA,$$

$$\boldsymbol{r}_3^m = \frac{t}{2} \int_A \left(\frac{1+\eta}{2} \xi\right) \boldsymbol{R}_b^T \boldsymbol{Q} \boldsymbol{\sigma} dA, \quad \boldsymbol{r}_4^m = \frac{t}{2} \int_A \left(\frac{1-\eta}{2} \xi\right) \boldsymbol{R}_b^T \boldsymbol{Q} \boldsymbol{\sigma} dA. \tag{16}$$

In the implementation these integrals are evaluated using 4-point Gaussian quadrature, where the integration point locations are given by

$$\xi_* = \left[-\frac{1}{\sqrt{3}}, \frac{1}{\sqrt{3}}, \frac{1}{\sqrt{3}}, -\frac{1}{\sqrt{3}}\right],$$

$$\eta_* = \left[-\frac{1}{\sqrt{3}}, -\frac{1}{\sqrt{3}}, \frac{1}{\sqrt{3}}, \frac{1}{\sqrt{3}}\right]. \tag{17}$$

Thus an integral is evaluated as

$$\int_A \phi(\xi,\eta)\boldsymbol{\sigma}dA \approx \sum_{i=1}^{4} \phi(\xi_i,\eta_i)\boldsymbol{\sigma}_i A_i, \tag{18}$$

where ϕ is an arbitrary function of the iso-parametric coordinates, A_i in the right hand side stands for the area of the cohesive layer and $\boldsymbol{\sigma}_i$ is the cohesive interface stress, both evaluated at and with respect to integration point i.

3.4 Drilling constraint

From (5) and Figure 1, it is evident that rotational velocities with respect to the adjacent shell normals will not induce translational velocities in the integration points, so a stabilization scheme is applied. To this end, introduce the generalized drilling strains δ_i^n and δ_j^m, $i = 1,2$, $j = 3,4$. These are distances that are incremented by their respective velocities

$$\dot{\delta}_i^n = \boldsymbol{n}_t^T\{\boldsymbol{\omega}_i^n d_{21} - \boldsymbol{R}_{21}(\dot{\boldsymbol{x}}_2^n - \dot{\boldsymbol{x}}_1^n)\}, \qquad i = 1,2,$$

$$\dot{\delta}_j^m = \boldsymbol{n}_b^T\{\boldsymbol{\omega}_j^m d_{34} - \boldsymbol{R}_{34}(\dot{\boldsymbol{x}}_3^m - \dot{\boldsymbol{x}}_4^m)\}, \qquad j = 3,4, \tag{19}$$

where

$$d_{21} = |\boldsymbol{x}_2^n - \boldsymbol{x}_1^n|,$$

$$d_{34} = |\boldsymbol{x}_3^m - \boldsymbol{x}_4^m|, \tag{20}$$

and for an arbitrary vector $\mathbf{v}$,

$$\boldsymbol{R}_{21}\boldsymbol{v} = \frac{1}{d_{21}}(\boldsymbol{x}_2^n - \boldsymbol{x}_1^n) \times \boldsymbol{v},$$

$$\boldsymbol{R}_{34}\boldsymbol{v} = \frac{1}{d_{34}}(\boldsymbol{x}_3^m - \boldsymbol{x}_4^m) \times \boldsymbol{v}. \tag{21}$$

A characteristic material stiffness E, typically a fraction of the elastic stiffness of the underlying cohesive material, is used to set up the drilling stress

$$\varsigma_i^n = E\delta_i^n, \qquad i = 1,2,$$

$$\varsigma_j^m = E\delta_j^m, \qquad j = 3,4, \tag{22}$$

and the stabilization nodal forces and moments are evaluated as

$$\mathbf{f}_1^n = A(\varsigma_1^n + \varsigma_2^n)\mathbf{R}_{21}^T\mathbf{n}_t, \qquad \mathbf{f}_2^n = -\mathbf{f}_1^n, \qquad \mathbf{f}_3^m = -\mathbf{f}_4^m, \qquad \mathbf{f}_4^m = A(\varsigma_3^m + \varsigma_4^m)\mathbf{R}_{34}^T\mathbf{n}_b, \tag{23}$$

and

$$\mathbf{r}_1^n = A\varsigma_1^n d_{21}\mathbf{n}_t, \qquad \mathbf{r}_2^n = A\varsigma_2^n d_{21}\mathbf{n}_t, \qquad \mathbf{r}_3^m = A\varsigma_3^m d_{34}\mathbf{n}_b, \qquad \mathbf{r}_4^m = A\varsigma_4^m d_{34}\mathbf{n}_b, \tag{24}$$

which are added to the structural counterparts in previous section.

4 Numerical Examples

Two different examples are here presented to verify the accuracy and robustness of shell element 29.

4.1   Separation of single layer

In this example the cohesive shell 29 is compared with the existing cohesive solid element 20. To do a fair comparison, each neighbor of the cohesive element consist of stacked elements: two bricks (thickness 0.05) with a thin shell layer (thickness 1E-6) in-between. The stacked elements are joined in thickness direction by nodal rigid bodies, and thus each stack act as a single brick of thickness 0.100001. The stacks can be joined by either a cohesive solid or a cohesive shell with thickness equal to the stacks, i.e. 0.100001. All elements in the stack share the same material data, in this case ***MAT_ELASTIC** with **RO=1E-3, E=1E5, PR=0.3**. The cohesive elements use ***MAT_COHESIVE_ELASTIC** with **EN=ET=1E5**. The simple bending test, in Figure 3, shows good agreement between solid and shell cohesive elements. In Figure 4, a similar test with simultaneous bending and pulling can be seen.
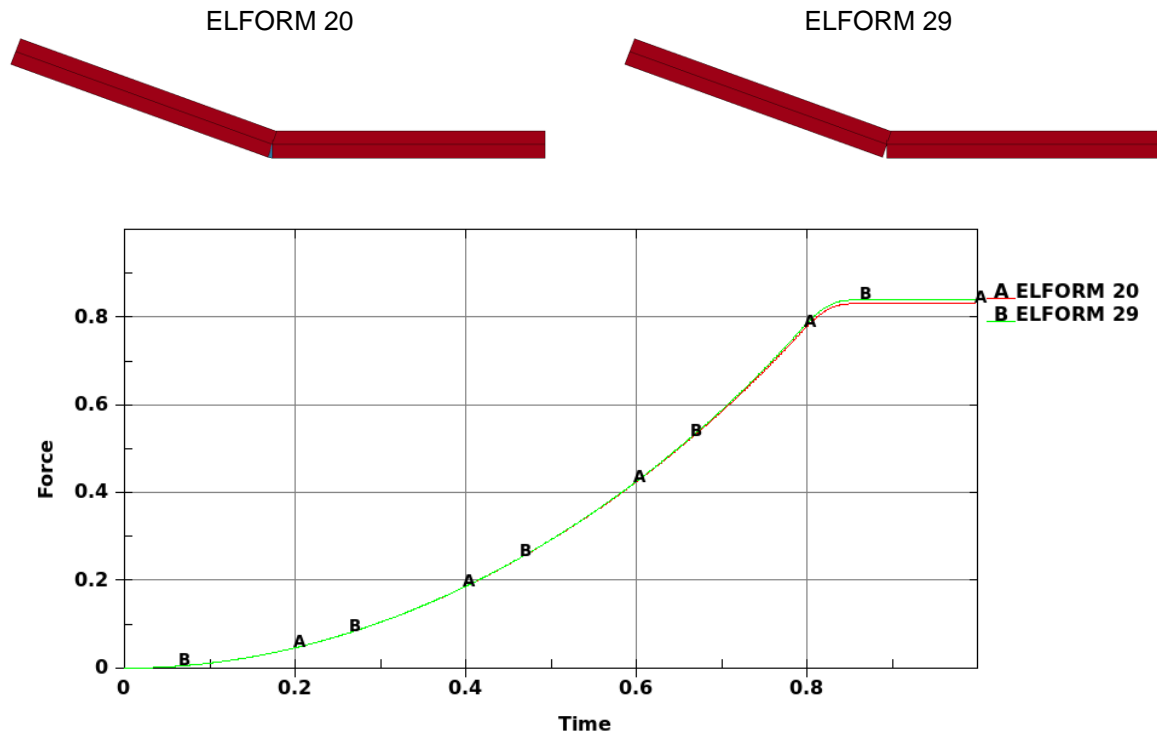
ELFORM 20   ELFORM 29

Fig.3:   Comparison between cohesive solid 20 and cohesive shell 29 for simple bending. Here, the prescribed boundary motion is zero after t=0.85.

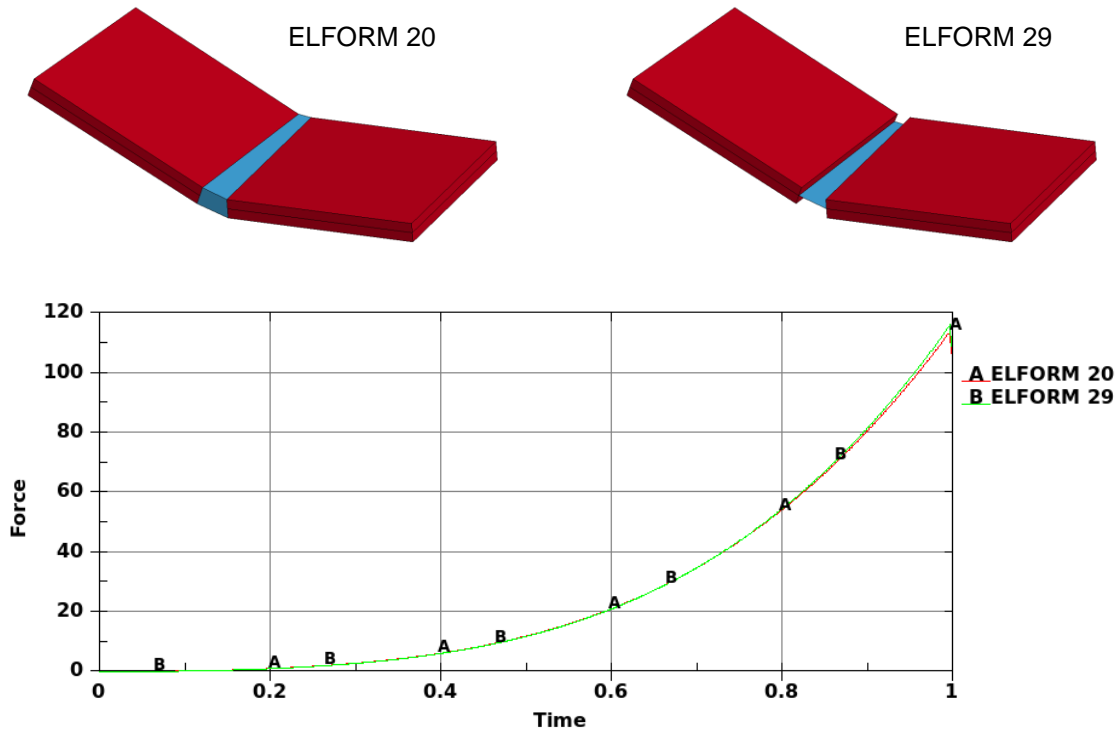Fig.4: *Comparison between cohesive solid 20 and cohesive shell 29 for bending and pulling.*

4.2 Notch in clamped plate

This example was treated experimentally in [1], and most recently in [5,6], where it was analyzed using extended finite element methods (XFEM). It deals with a pre-notched clamped plate with length and width 203 mm and thickness 0.8 mm. The initial crack is 40 mm deep and a transverse displacement of 20 m/s is applied to the outer corners of the crack. A line of cohesive shells is place in the middle of the plate in line with the initial crack. The material is here the rate independent part of ***MAT_SIMPLIFIED_JOHNSON_COOK** and the cohesive material is given by the simple bi-linear elastic model in ***MAT_COHESIVE_MIXED_MODE**, see material data in Figure 5.

```
*MAT_SIMPLIFIED_JOHNSON_COOK
$#     mid         ro          e         pr         vp
         1     7.85E-6      210.0        0.3        0.0
$#       a          b          n          c
     0.175      0.767     0.6722        0.0


*MAT_COHESIVE_MIXED_MODE
$#     mid         ro      roflg    intfail         en         et        gic       giic
         2     7.85E-6        1.0        4.0      210.0      210.0       0.25       0.25
$#     xmu          t          s        und        utd
       1.0      0.306      0.306      1.634      1.634
```

Fig.5: *LS-DYNA input cards in unit system mm/ms/kg/kN*

In Figure 6, the mesh and deformed plate is visualized at final time, and in Figure 6 a comparison is made with experimental data from [1] and the XFEM result from [5]. The cohesive element approach show good agreement with both data and XFEM.
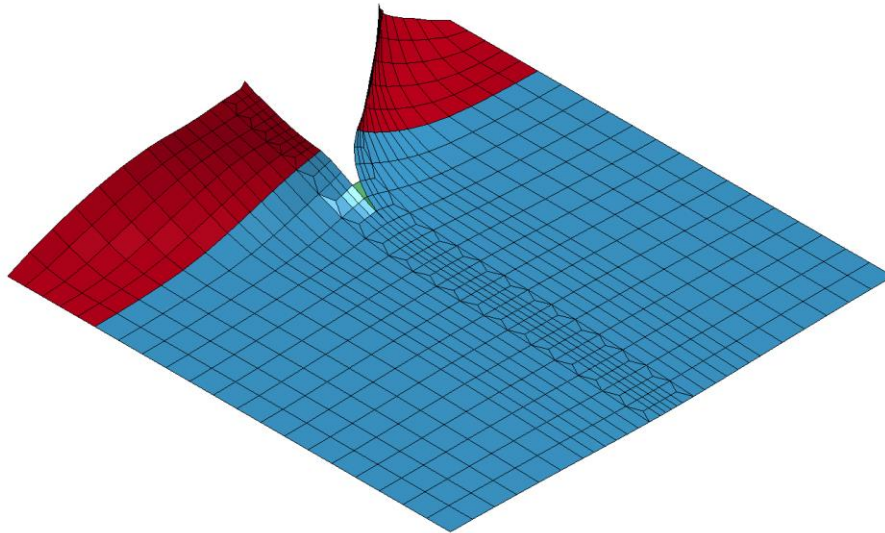
Fig.6: Deformed plate.The initial 40 mm crack cuts through the red area where no cohesive elements are present. Note that three cohesive elements has eroded in the blue area.
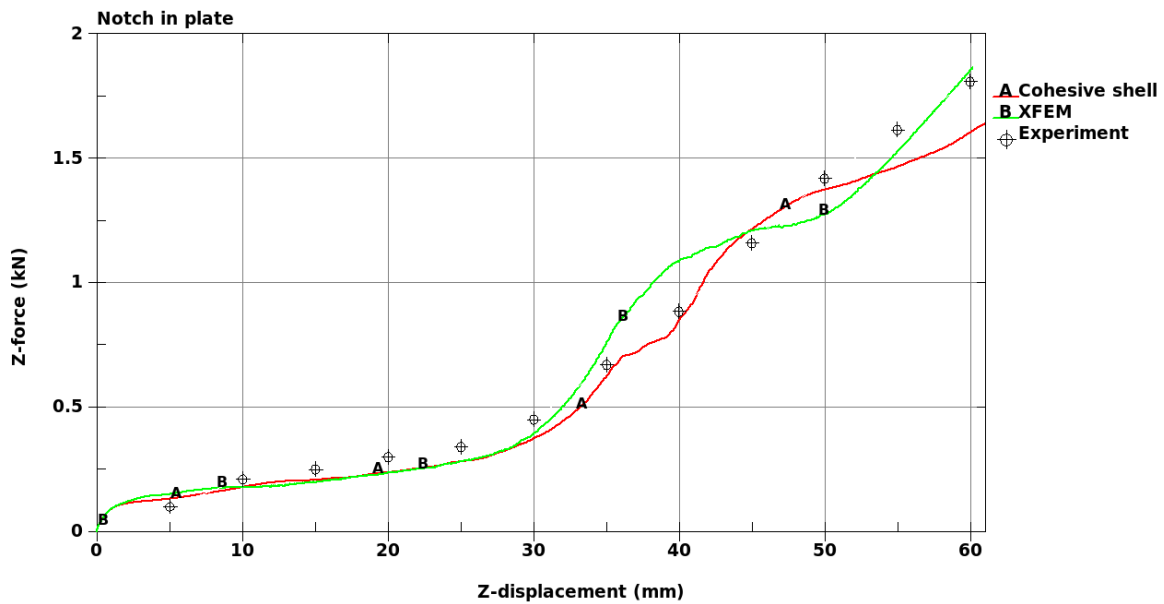

Fig.7: Comparison with the experimental data from [1] and the XFEM result from [5]. The plot shows the sum of the transversal force response on the displaced boundary nodes.

5 Conclusion

As of Revision 8.0 a new cohesive shell element is available for edge-to-edge connection of quadrilateral thin shells. The new cohesive element (type 29) accounts for in-plane and out-of-plane separation as well as hinge bending and works with existing cohesive material models. It shows good agreement with existing solid cohesive elements (type 19 and 20), as well as with experimental data and the XFEM method for the example of crack propagation in a pre-notched clamped plate.

6 Literature

[1]   Areias PMA, Belytschko T: "Non-linear analysis of shells with arbitrary evolving cracks using XFEM", International Journal for Numerical Methods in Engineering, 62, 2005, 384-415

[2]   Cirak F, Deiterding R, Sean SP: "Large-scale fluid-structure interaction simulation of viscoplastic and fracturing thin-shells subjected to shocks and detonations", Computers and Structures, 85, 2007, 1049-1065

[3]   Cirak F, Ortiz M, Pandolfi A: "A cohesive approach to thin-shell fracture and fragmentation", Computer Methods in Applied Mechanics and Engineering, 194, 2005, 2604-2618

[4]   Cornec A: "Application of the cohesive model for predicting the residual strength of a large scale fuselage structure with a two-bay crack", Engineering Failure Analysis, 16, 2009, 2541-2558

[5]   Mostofizadeh S, Fagerström M, Larsson R: "Dynamic crack propagation in elastoplastic thin-walled structures: Modelling and validation", Int. J. Numer. Meth. Engng, 96(2), 2013, 63-128

[6]   Muscat-Fenech CM, Atkins AG: "Out-of-plane stretching and tearing fracture in ductile sheet materials", International Journal of Fracture, 84, 1997, 297-306

[7]   Scheider I, Brocks W: "Residual strength prediction of a complex structure using crack extension analyses", Engineering Fracture Mechanics, 76, 2009,149-163

[8]   Zavattieri PD: "Modeling of crack propagation in thin-walled structures using a cohesive model for shell elements", Journal of Applied Mechanics, 73, 2006, 948-958